



1 **A novel framework for accurately quantifying wetland**  
2 **depression water storage capacity with coarse-resolution**  
3 **terrain data**

4 Boting Hu<sup>1,2</sup>, Liwen Chen<sup>1</sup>, Yanfeng Wu<sup>1</sup>, Jingxuan Sun<sup>1,2</sup>, Y. Jun Xu<sup>3</sup>, Qingsong  
5 Zhang<sup>1,2</sup>, Guangxin Zhang<sup>1</sup>

6 <sup>1</sup> Northeast Institute of Geography and Agroecology, Chinese Academy of Sciences, Changchun, Jilin  
7 130102, China

8 <sup>2</sup> University of Chinese Academy of Sciences, Beijing 100049, China

9 <sup>3</sup> School of Renewable Natural Resources, Louisiana State University Agricultural Center, 227  
10 Highland Road, Baton Rouge, LA 70803, USA

11 *Correspondence to:* Guangxin Zhang (zhgx@iga.ac.cn)

12

13 **Abstract.** Accurate quantification of wetland depression water storage capacity (WDWSC) is  
14 imperative for comprehending the wetland hydrological regulation functions to support integrated  
15 water resources management. Considering the challenges posed by the high acquisition cost of  
16 high-resolution LiDAR DEM or the absence of field measurements for most wetland areas, urgent  
17 attention is required to develop an accurate estimation framework for WDWSC using open-source,  
18 low-cost, multi-source remote sensing data. In response, we developed a novel framework,  
19 WetlandSCB, utilizing coarse-resolution terrain data for accurate estimation of WDWSC. This  
20 framework overcame several technical difficulties, including biases in above-water topography,  
21 incompleteness and inaccuracy of wetland depression identification, and the absence of bathymetry.  
22 Validation and application of the framework were conducted in two national nature reserves of  
23 northeast China. The study demonstrated that integrating priority-flood algorithm, morphological  
24 operators and prior information can accurately delineate the wetland depression distribution with  
25 overall accuracy and Kappa coefficient both exceeding 0.95. The use of water occurrence map can  
26 effectively correct numerical biases in above-water topography with Pearson coefficient and  $R^2$   
27 increasing by 0.33 and 0.38 respectively. Coupling spatial prediction and modeling with remote sensing  
28 techniques yielded highly accurate bathymetry estimates, with <3% relative error compared to filed  
29 measurements. Overall, the WetlandSCB framework achieved estimation of WDWSC with <10%



30 relative error compared to field topographic and bathymetric measurements. The framework and its  
31 concept are transferable to other wetland areas globally where field measurements and/or  
32 high-resolution terrain data are unavailable, contributing to a major technical advancement in  
33 estimating WDWSC in river basins.

34 **Keywords:** Wetland depression; Water storage capacity; Hypsometric curve; coarse-resolution  
35 terrain data; wetland hydrological regulation functions

36

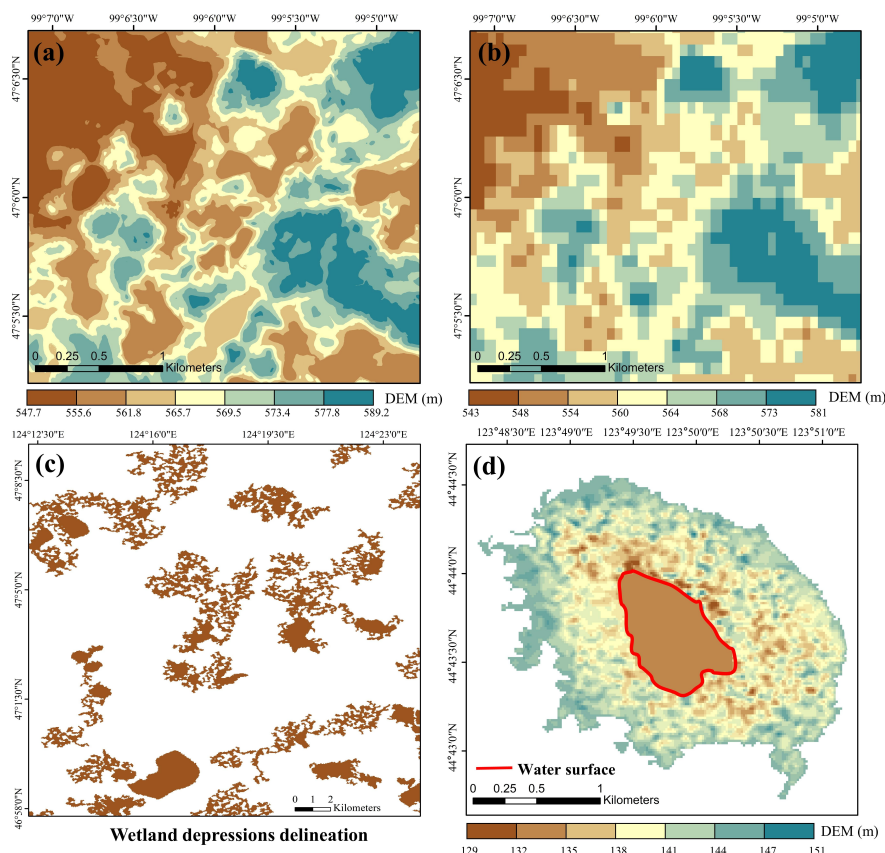
## 37 1 Introduction

38 Wetlands are multifunctional ecosystems considered as nature-based solutions for effective water  
39 management in river basins (Thorslund et al., 2017). They exert a profound influence on watershed  
40 hydrological processes and water resource availability through their hydrological regulation functions,  
41 such as maintaining baseflow, buffering floods, and delaying droughts (Acreman and Holden, 2013;  
42 Wu et al., 2023). These functions are essential for enhancing watershed resilience and ensuring water  
43 security (Cohen et al., 2016; Evenson et al., 2018; Lane et al., 2018). Wetland depression water storage  
44 capacity (hereafter abbreviated as WDWSC) represents a critical component of wetland hydrological  
45 regulation functions. The quantitative study of the WDWSC to advance scientific insights into wetland  
46 hydrological regulation functions and support integrated water resources management (Ahmad et al.,  
47 2020; Fang et al., 2019; Jones et al., 2018; Shook et al., 2021).

48 The WDWSC can be defined as the maximum surface water volume that each wetland depression  
49 can store without spilling to down-gradient waters (Jones et al., 2018). Previous studies predominantly  
50 employed wetland depression identification algorithms to derive wetland depression topography from  
51 terrain data. Subsequently, hypsometric curves (area-depth) are constructed based on the derived  
52 topography. Finally, the integration of the hypsometric curves is solved to determine the WDWSC (e.g.,  
53 Haag et al., 2005; Wu and Lane, 2016). Therefore, the key determinants for the accuracy of the  
54 WDWSC calculation are the rationality of the wetland depression identification algorithms and the  
55 precision of terrain data. Many scholars have conducted research on wetland depression identification  
56 algorithms, which can be mainly categorized into three types: depression filling, depression breaching  
57 and hybrid combining both the filling and breaching approaches. Among these, the priority-flood  
58 algorithm within the depression filling category is widely adopted as a prevalent algorithm for wetland  
59 depression identification (Barnes et al., 2014; Lindsay, 2016; Wu et al., 2019; Zhou et al., 2016). The



60 priority-flood algorithm works by flooding DEM cells inwards from their edges using a priority queue  
61 to determine the sequence of cells to be flooded. Wu et al. (2019) and Rajib et al. (2019) demonstrated  
62 the feasibility of accurately deriving wetland depression topography using the priority-flood algorithm  
63 in the Pipestem watershed and Upper Mississippi river basin, respectively. Bare-earth high-resolution  
64 airborne light detection and ranging (LiDAR) DEM can provide accurate topographic information of  
65 wetland depressions, significantly improving the estimation accuracy of the WDWSC. For example,  
66 Jones et al. (2018) used high-resolution LiDAR DEM to estimate WDWSC in the Delmarva Peninsula.  
67 However, the high acquisition cost of LiDAR DEM renders it impractical for large-scale estimation of  
68 WDWSC. The global open-access spaceborne-derived DEMs (hereafter referred as global DEMs),  
69 such as Shuttle Radar Topography Mission (SRTM), ALOS Global Digital Surface Model, the Terra  
70 Advanced Spaceborne Thermal Emission and Reflection Radiometer (ASTER) Global Digital  
71 Elevation Model, offer topographic information at a fine spatial scale. However, compared to the  
72 bare-earth LiDAR DEM, the global DEMs exhibit three obvious limitations. First, radar altimetry  
73 cannot penetrate water surfaces, so the global DEMs produced from radar altimetry do not provide any  
74 bathymetric information. Second, in certain regions, there may be substantial numerical discrepancies  
75 in above-water topography. Third, the global DEMs often suffer from lower horizontal and vertical  
76 resolutions. Due to the limitations in global DEMs, delineation of wetland depressional areas using the  
77 advanced priority-flood algorithm also suffers from three problems: the bias in above-water topography  
78 (Fig. 1a and 1b), incompleteness and inaccuracy of wetland depressions identification (Fig. 1c), and the  
79 absence of bathymetric information (Fig. 1d).



80  
81 **Figure 1: Wetland depression extraction based on the priority-flood algorithm and global DEMs suffers**  
82 **from the bias of above-water topography (Figures 1a and 1b show the discrepancies in above-water**  
83 **topography obtained from LiDAR DEM and ALOS DEM, respectively, in the Prairie Pothole Region of**  
84 **North Dakota), incompleteness and inaccuracy of wetland depressions identification (Fig. 1c), and the**  
85 **absence of bathymetric information in figure 1d, where the entire water surface is represented by a single**  
86 **elevation value of 129 m).**

87  
88 In an effort to minimize the impact of the absence of bathymetric information in global DEMs on  
89 the estimation accuracy of the WDWSC, researchers have conducted studies on the estimation of  
90 underwater hypsometric relationship of wetland depressions, and the methods can be divided into two  
91 types: spatial prediction and modeling methods and remote sensing technologies. The spatial prediction  
92 and modeling methods assume that the bathymetry can be considered as a spatial extension of the



93 surrounding exposed terrains due to long-term tectonic and geophysical evolution processes.  
94 Consequently, the underwater hypsometric relationship is assumed to be fundamentally similar to the  
95 above-water hypsometric relationship in wetland depressions (e.g., Ahmad et al., 2020; Bonnema et al.,  
96 2016; Bonnema and Hossain, 2017; Liu and Song, 2022; Tsai et al., 2010; Vanthof and Kelly, 2019;  
97 Verones et al., 2013; Wu and Lane, 2016; Xiong et al., 2021). However, the large numerical bias in the  
98 above-water topography of global DEMs in certain regions can distort the constructed above-water  
99 hypsometric relationship of wetland depressions, thus introducing significant uncertainty to the  
100 underwater hypsometric relationship estimated by this method. Over the past few decades, remote  
101 sensing technologies have demonstrated remarkable capabilities in estimating underwater hypsometric  
102 relationships at large spatial scales, facilitated by the rapid emergence of various advanced satellite  
103 sensors, including optical, passive microwave, and radar instruments (Duan and Bastiaanssen, 2013;  
104 Gao et al., 2015; Liu et al., 2022). The commonly employed approach for estimating underwater  
105 hypsometric relationship requires simultaneous observations of water area provided by optical images  
106 (e.g., Landsat series) and the corresponding water level provided by altimetry satellites (e.g., Sentinel-3,  
107 CryoSat-2, Envisat). However, accuracy challenges arise due to numerical biases of altimetry satellites,  
108 cloud contamination in some optical images, and the occasional occurrence of one water area value  
109 corresponding to multiple water level values or vice versa (Li et al., 2019a; Liu et al., 2024). In  
110 summary, previous studies have mainly utilized LiDAR DEM data to estimate WDWSC (e.g., Jones et  
111 al., 2018; Huang et al., 2011; Kessler and Gupta, 2015; Land and D'Amico, 2010; Wu et al., 2016; Wu  
112 et al., 2019). However, these studies have seriously overlooked the issues of incompleteness and  
113 inaccuracy of wetland depression identification, as well as the bias in above-water topography,  
114 resulting in a high level of uncertainty in the WDWSC estimation. In addition, insufficient attention has  
115 been paid to the drawbacks and limitations of both spatial prediction and modeling methods and remote  
116 sensing technologies in estimating bathymetry. Consequently, a comprehensive and systematic solution  
117 for the accuracy estimation of WDWSC based on the global DEMs has not yet been developed.

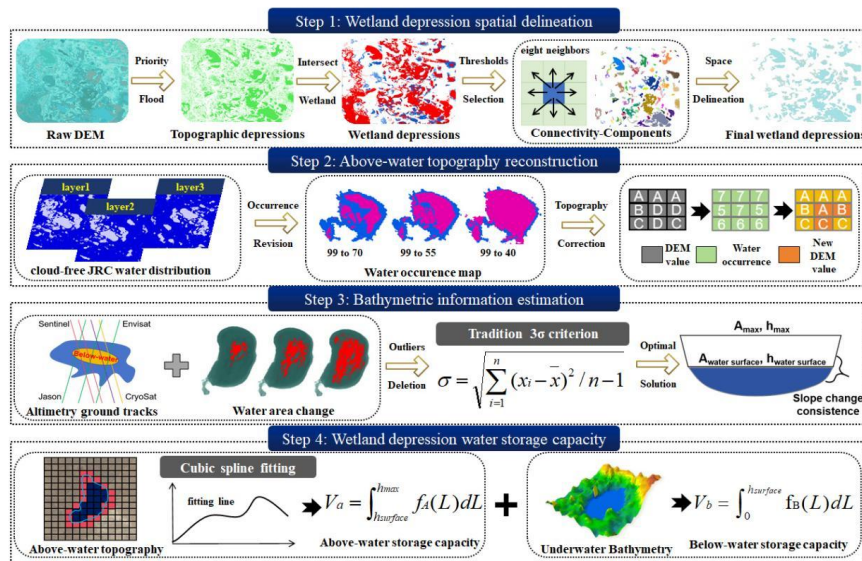
118 Therefore, this study aims to develop a framework for accurately estimating WDWSC by  
119 integrating multi-source remote sensing data and prior knowledge. Specifically, we integrated  
120 priority-flood algorithm, morphological operators and prior information on water distribution map to  
121 delineate the spatial extent of wetland depressional areas. We then corrected the bias in above-water  
122 topography based on water occurrence map. Finally, we utilized remote sensing techniques to couple



123 spatial prediction and modeling to estimate bathymetry of wetland depressional areas. The principle  
 124 contribution of this developed framework, termed as WetlandSCB, lies in addressing the challenges  
 125 hindering the improvement of accuracy in estimating WDWSC based on global DEMs.

## 126 2 Methodology

127 The WetlandSCB framework can be summarized in four steps as illustrated in Figure 2. Step 1  
 128 delineation of wetland depressional areas; Step 2 above-water topography reconstruction; Step 3  
 129 bathymetric information estimation; and Step 4 hypsometric curve construction and WDWSC  
 130 calculation. Each of the four steps are described in the following sections.



131  
 132 **Figure 2: Flowchart of the WetlandSCB framework for accurate estimation of wetland depression water**  
 133 **storage capacity (WDWSC) comprising four technical steps. In step 1, spatial distribution of wetland**  
 134 **depressional areas are delineated. In step 2, wetland above-water topography is reconstruction. In step 3,**  
 135 **bathymetric information of wetland depressional areas is estimated. In step 4, a hypsometric curve (i.e.**  
 136 **depth-area relation) is developed and WDWSC is quantified.**

137

### 138 2.1 Wetland depression spatial delineation

139 We extracted the original wetland depression map from the global DEMs based on the  
 140 priority-flood algorithm and wetland maps (Fig. 3). To eliminate the artifact wetland depressions, it  
 141 was necessary to transform the wetland depression map into a binary image consisting of pixels that

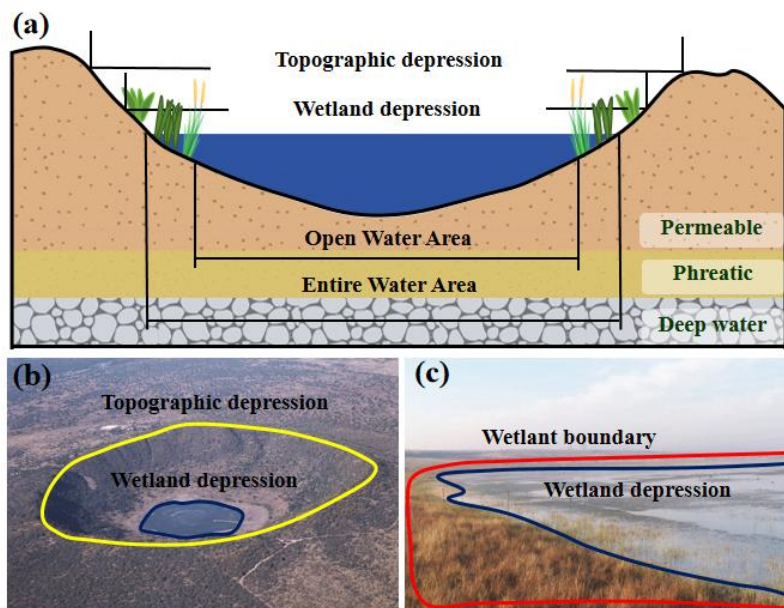


142 area labeled as logical ones (wetland depression) and zeros (non-wetland depression). We then  
143 employed the eight-neighbor connectivity algorithm to extract the spatial extent of each wetland  
144 depression from the binary image. Subsequently, the circularity (Eq. 1) and eccentricity (Eq. 2)  
145 indicators were used to exclude the artifact wetland depressions (Ahmad et al., 2020) as follows:

146 
$$\text{Circularity} = \frac{P}{2\sqrt{\pi \cdot A}} \quad (1)$$

147 
$$\text{Eccentricity} = \frac{D_f}{L_m} \quad (2)$$

148 where  $P$  (m) and  $A$  (m<sup>2</sup>) are the perimeter and area of the wetland depression, respectively.  $D_f$  (m)  
149 and  $L_m$  (m) represent distance between foci and the length of major axis of wetland depression.



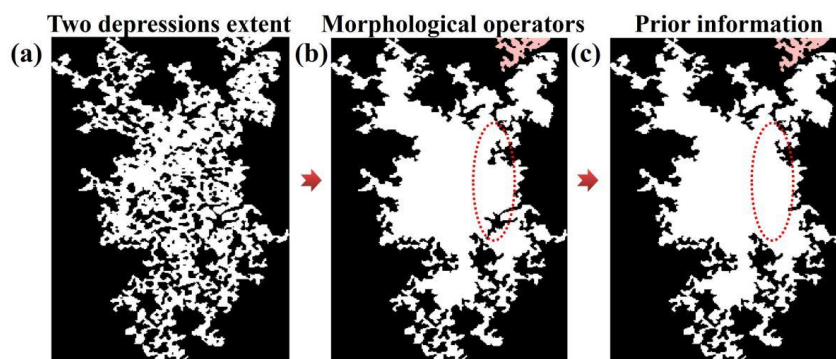
150  
151 **Figure 3.** (a) Conceptual diagram of wetland depression profile. (b) and (c) show the two representative  
152 wetland depressional areas located in South Africa (modified from De Klerk et al., 2016).

153  
154 Due to incompleteness and inaccuracy identification of some wetland depressions in the original  
155 wetland depression map (Figure 4a), morphological operators of erosion and dilation are applied for the  
156 initial spatial processes (Figure 4b). The erosion operator erodes away the boundaries of wetland  
157 depressions to enhance their edges and remove noise. The dilation operator fills up small holes  
158 (non-wetland depression pixels) surrounded by a group of wetland depression pixels (Pulvirenti et al.,





159 2011a). The combined effect of the two operators is to remove noises while preserving the substantive  
160 features in the image. The water distribution map, which serves as prior information, effectively  
161 characterizes the spatial extent of wetland depressions (Figure 3). Therefore, the wetland depression  
162 map, after being processed by the morphological operators, is then intersected with the water  
163 distribution map to obtain a complete and final wetland depression map (Figure 4c).  
164



165  
166 **Figure 4.** The wetland depression map based on the morphological operators and priori information on the  
167 water distribution map

## 169 2.2 Above-water topography reconstruction

170 The water occurrence map can effectively describe three-dimensional topography at a large spatial  
171 scale (Armon et al., 2020; Li et al., 2019b). The water occurrence map is generated by summing the  
172 times that the pixel is detected as water and dividing it by the number of total valid observations.  
173 Therefore, if there is a accurate water occurrence maps, a close relationship between the water  
174 occurrence and the topography for wetland depressions can be found (Li et al., 2021). The open-source  
175 Global Surface Water Mapping Layers produced by the European Commission's Joint Research Centre  
176 (JRC) contains a water occurrence map, which has been widely used to describe the topography of  
177 wetland depressions globally or in different regions (Luo et al., 2019; Pickens et al., 2020; Yao et al.,  
178 2019; Zou et al., 2018). However, due to the temporal discontinuity of cloud-free JRC water  
179 distribution images, they are more available during dry seasons than wet seasons, leading to deviations  
180 in the representation of real topography at the scale of individual wetland depression (Chu et al., 2020).

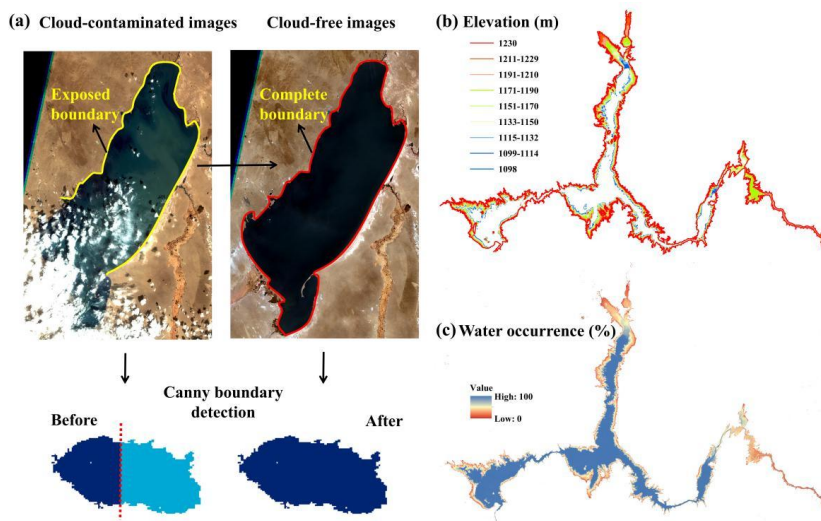
181 To address the above issue, this study proposes a method to restore the cloud-contaminated JRC





182 water distribution images to improve the accuracy of the JRC water occurrence map. For wetland  
183 depressional areas, the JRC water distribution images are classified into cloud-free and  
184 cloud-contaminated images using the cloud screening algorithm of the Google Earth Engine platform.  
185 The Canny edge detection algorithm is used to obtain the water body boundary of the two types of  
186 images. Theoretically, if the water areas are the same, the water body boundary of the cloud-free image  
187 should overlap with the exposed water body boundary in the cloud-contaminated image (Figure 5a).  
188 Therefore, by overlapping the water body boundaries of the cloud-free images with the  
189 cloud-contaminated images, the missing spatial extent of water bodies in the cloud-contaminated  
190 images can be filled.

191 The corrected JRC water occurrence map is utilized to reconstruct above-water topography. This  
192 is because the water occurrence values within the same wetland depression correspond to elevation  
193 values (Figure 5b and 5c). However, each corrected water occurrence value may correspond to multiple  
194 elevation values in the global DEMs. Therefore, the median of multiple elevation values is used as the  
195 unique elevation value corresponding to the water occurrence value.



196  
197 **Figure 5. Above-water topography reconstruction of wetland depressional areas. (a) Restoration method of**  
198 **cloud-contaminated JRC water distribution images. (b) LiDAR DEM and JRC water occurrence map of**  
199 **Mead Lakes in the United States.**

200

### 201 2.3 Bathymetric information estimation



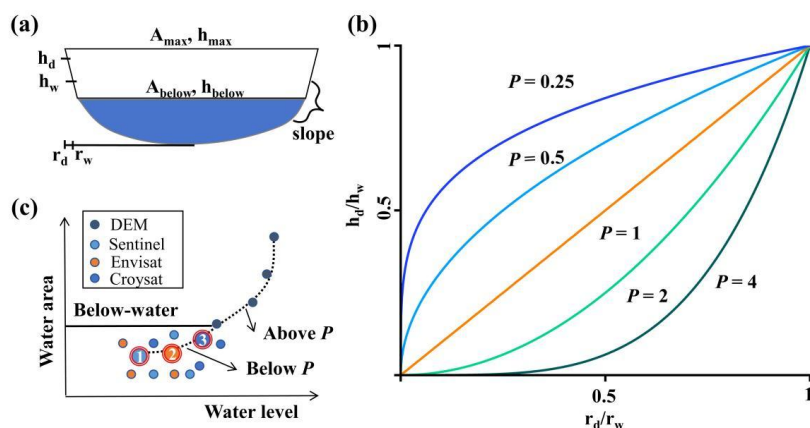
202 The remote sensing technologies are used to estimate the underwater bathymetry of wetland  
 203 depressions, and the similarity between the underwater and above-water hypsometric relationships is  
 204 served as an evaluation criterion to seek for the optimal solution within the estimated results that  
 205 accurately represents underwater bathymetry based on the principle of spatial prediction and modeling  
 206 methods.

207 The outliers in the underwater area-level pairs are removed using the 3-sigma rule. As the slope  
 208 profile is a crucial indicator reflecting the hypsometric relationship of wetland depressions (Clark and  
 209 Shook, 2022; Sjöberg et al., 2022). Therefore, we first form various combinations of the processed  
 210 underwater area-level pairs (each water area value uniquely corresponds to a water level value in each  
 211 combination), and calculate the slope profile value  $p_u$  for each combination. Then the combination with  
 212  $p_u$  closest to the above-water slope profile  $p_a$  is taken as the optimal solution, which can effectively  
 213 represent underwater bathymetry of wetland depressions.

214 In this study, a logarithmic transformation is applied to the calculation formula for the slope  
 215 profile  $p$  of wetland depressions established by Hayashi and Van der Kamp (2000) to obtain Eq. 3. The  
 216 least squares method is used to solve Eq. 3 to obtain the slope profile  $p$  value of wetland depressions:

$$217 \quad P = \frac{2 \cdot \ln(h_w / h_d)}{\ln(A_w / A_d)} \quad (3)$$

218 where  $h$  (m),  $A$  (m<sup>2</sup>) represent the depth and area of wetland depressions, and  $w$  and  $d$  represent  
 219 the different area-depth pairs.



220  
 221 **Figure 6. Estimation of bathymetric information for wetland depressional areas. (a) Schematic**  
 222 **representation of a simplified wetland depression profile, where  $h$  (m),  $r$  (m) and  $A$  (m<sup>2</sup>) represent the depth**



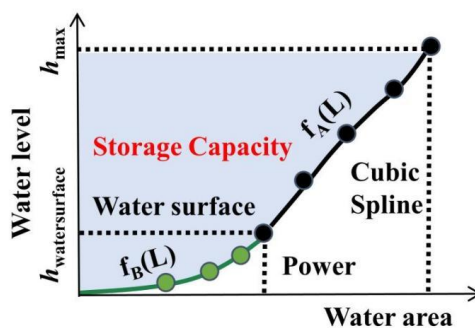
223 of a wetland depressional area, the distance between the edge and the center of the wetland depression, and  
224 the area of the wetland depression, respectively. (b) Wetland depression profile for various  $p$  values. (c)  
225 Methods for bathymetric estimation of wetland depressions, where Sentinel, Envisat, and Croysat are  
226 different altimetry satellites, and the numbers 1, 2, and 3 are selected depth-area pairs.

227

#### 228 2.4 Estimation of wetland depression water storage capacity

229 Deriving the area-level hypsometric relationship from the corrected above-water topography and  
230 estimated underwater bathymetry of wetland depressions. The monotonic cubic spline and power  
231 function are employed to fit the hypsometric relationships (i.e., depth-area relations) to derive the  
232 above-water hypsometric curve  $f_A(L)$  and the underwater hypsometric curve  $f_B(L)$  (Messenger et al.,  
233 2016; Yao et al., 2018), respectively. Subsequently, the integration of these two curves (Figure 7) is  
234 performed to calculate the WDWSC, represented as  $V$  in Eq. 4:

$$235 \quad V = \int_{h_{\text{watersurface}}}^{h_{\text{max}}} f_A(L) dL + \int_0^{h_{\text{watersurface}}} f_B(L) dL \quad (4)$$



236

237 Figure 7. Schematic diagram for the estimation of wetland depression water storage capacity. Two  
238 depth-area rating curves are applied for the bathymetric volume and the above-water topographic volume.

239

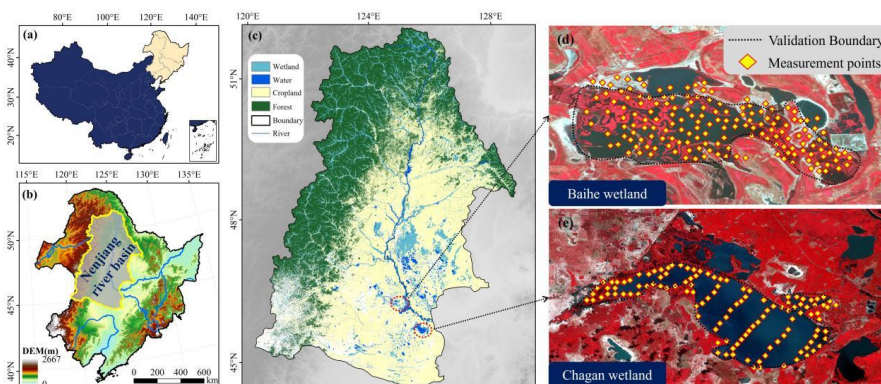
### 240 3 Validation sites and datasets

#### 241 3.1 Validation sites

242 We applied the WetlandSCB to two wetlands in the Nenjiang River Basin (NRB), northeast China,  
243 to validate the framework. Draining a total area of 297,100 km<sup>2</sup>, the NRB is one of the largest river  
244 basins in north China. In this river basin, agricultural lands and wetlands (lakes and swamps) are  
245 prevalent (Wu et al., 2023). Recognised as critical regulators of the water balance within the NRB,  
246 wetlands are considered more important than other ecosystems in mitigating future hydrological



247 extremes and increasing water availability for agriculture (Chen et al., 2020, Wu et al., 2020a, Wu et al.,  
248 2020b, Wu et al., 2020c). For method validation and application of the WetlandSCB framework, we  
249 focused on two national nature reserves within the NRB: the Baihe Lake and the Chagan Lake. The  
250 Baihe Lake, characterised as a marsh wetland, covers approximately 40 km<sup>2</sup>, predominantly  
251 comprising seasonal inundation zones, with an average water depth of less than 1 m. In contrast, The  
252 Chagan Lake is a large lacustrine wetland of about 372 km<sup>2</sup>, mainly composed of perennial inundation  
253 zones, with an average water depth of 2.5 m. These two validation wetlands represent different  
254 characteristics in terms of type, area, and average water depth to verify the application robustness of  
255 our developed framework. Field measurements of topographic and bathymetric information (elevation  
256 and depth) were conducted for both the Baihe Lake and the Chagan Lake, consisting of 248 and 657  
257 measurement points, respectively (Figure 8).



258  
259 **Figure 8. Locations and distribution of elevation and depth measurements across the Baihe Lake and**  
260 **Chagan Lake in the Nenjiang River basin, northeast China.**

261

### 262 3.2 Datasets

263 The application of the WetlandSCB framework requires the following data: (i) the global DEMs  
264 sourced from SRTM DEM, with water distribution map sourced from the accompanying SRTM Water  
265 Body Data (<https://earthexplorer.usgs.gov/>); (ii) wetland maps extracted from the 30-m resolution land  
266 cover data for the years 1990-2019 (<https://zenodo.org/records/5816591>, Yang and Huang, 2021) and  
267 30-m resolution wetland map in 2015 year (<http://northeast.geodata.cn/index.html>, Mao et al., 2020).  
268 This study overlays the data from both sources to reduce the uncertainties in the wetland maps; (iii)  
269 water distribution maps and water occurrence map obtained from the Global Surface Water datasets



270 (<https://earthengine.google.com>, Pekel et al., 2016); (iv) altimetry satellite data sourced from the  
271 Sentinel-3A/3B products (<https://scihub.copernicus.eu/>). In addition, pre-processing of Sentinel-3  
272 altimetry data is performed using the geophysical and atmospheric correction method developed by  
273 Huang et al. (2019) (Eq. 5 and Eq. 6) to improve data accuracy:

$$274 \quad H_{waterlevel} = H_{alt} - R - Cor \quad (5)$$

275 where  $H_{waterlevel}$  is the water level referenced to the EGM96 geoid,  $H_{alt}$  is the altitude of the  
276 altimeter derived from the modeling of satellite trajectory,  $R$  is the range computed through the time  
277 duration of the echoes, and  $Cor$  is referred to as the geophysical and environmental corrections:

$$278 \quad Cor = C_{dry} + C_{wet} + C_{iono} + C_{solidEarth} + C_{pole} + C_{EGM96} \quad (6)$$

279 where  $C_{dry}$ ,  $C_{wet}$ ,  $C_{iono}$ ,  $C_{solidEarth}$ ,  $C_{pole}$  and  $C_{EGM96}$  are the dry tropospheric, wet tropospheric,  
280 ionospheric corrections, the solid Earth tide, polar tide corrections and the EGM96 geoid respectively.

## 281 4 Results and discussions

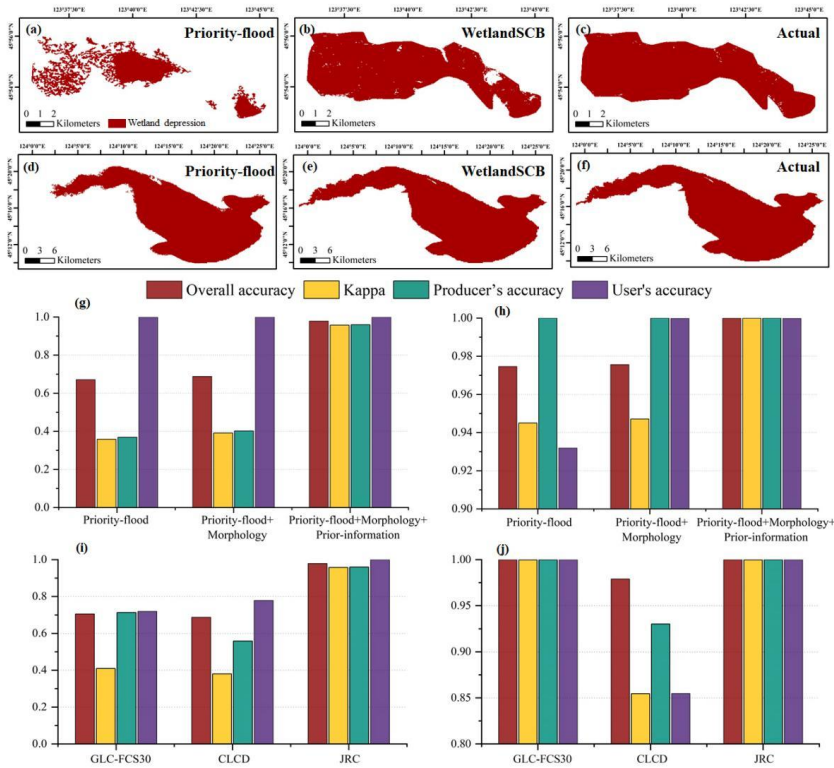
### 282 4.1 Performance evaluation of wetland depression spatial delineation and uncertainty analysis

283 The performance of wetland depression spatial delineation based on the WetlandSCB framework  
284 was evaluated using four indicators: overall accuracy, kappa coefficient, producer's accuracy, and user's  
285 accuracy (Fig. 9a-f). The results indicate that the WetlandSCB framework can accurately determine the  
286 spatial distribution of wetland depressions, with all four indicators exceeding 0.95. In contrast, the  
287 user's accuracy is above 0.93 in both validation wetlands (error of commission is 0.07), and the  
288 producer's accuracy is only 0.37 (error of omission is 0.63) in Baihe Lake based on the priority-flood  
289 algorithm. The findings suggest that the algorithm can effectively identify wetland depressions, but is  
290 limited by the numerical errors of the global DEMs, which leads to lower extraction accuracy of the  
291 spatial distribution of wetland depressions (Zhou et al., 2016). In comparison, the WetlandSCB  
292 framework outperforms the priority-flood algorithm in wetland depression spatial delineation.

293 Uncertainty in wetland depression spatial delineation using the WetlandSCB framework primarily  
294 mainly arises from morphological operators and prior information on water distribution map. Figures  
295 9g and 9h show that, compared with morphological operators, prior information on water distribution  
296 map can significantly alter the performance of wetland depression spatial delineation and is a key  
297 factor in determining the level of uncertainty. For instance, in Baihe Lake, the overall accuracy and  
298 kappa coefficient improved by 0.29 and 0.56, respectively, after processing with prior information on



299 water distribution map. Similar studies have also found that the type and reliability of prior information  
 300 are major factors affecting the spatial filling performance of surface water maps (Aires, 2020;  
 301 Pulvirenti et al., 2011b). Therefore, this study compared the wetland depression spatial delineation  
 302 results based on three sets of prior information on water distribution map: GLC-FCS30 (from Yang et al., 2021),  
 303 CLCD (from Yang and Huang, 2021), and JRC (Fig. 9i and 9j). The overall accuracy  
 304 differences for the Baihe Lake and Chagan Lake ranged from 0.68 to 0.98 and from 0.94 to 0.99,  
 305 respectively. In general, the accuracy levels of prior information from high to low were JRC >  
 306 GLC-FCS30 > CLCD. This suggests that selecting highly reliable prior information on water  
 307 distribution map is an essential way to reduce uncertainty in the WetlandSCB framework.



308  
 309 Figure 9. (a), (b), and (c) show the spatial distribution of wetland depression areas in the Baihe Lake  
 310 based on the priority-flood algorithm, WetlandSCB framework, and field measurements, respectively. (d),  
 311 (e), and (f) show the corresponding results for the Chagan Lake. The impact of morphological operators and  
 312 prior information on water distribution map from the WetlandSCB framework is illustrated in (g) and (h).  
 313 The influence of different prior information on water distribution map from the WetlandSCB framework is



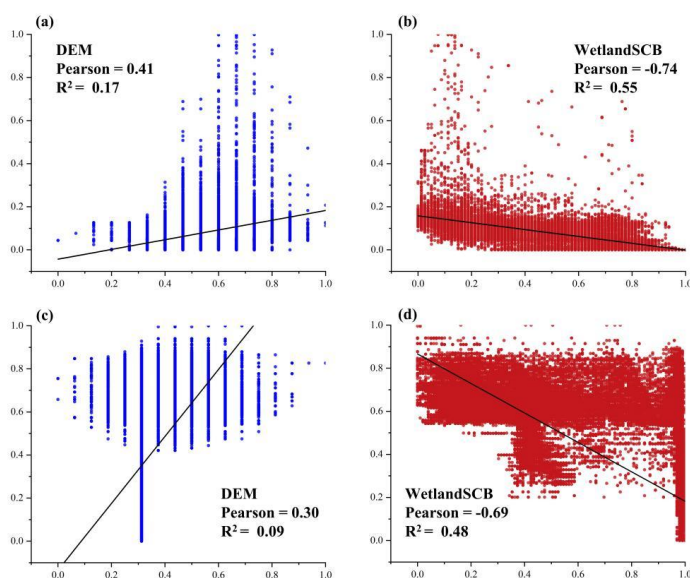


314 presented in (i) and (j).

315

#### 316 4.2 Performance evaluation of above-water topography correction and uncertainty analysis

317 The consistency between the original and corrected above-water topography and the actual  
318 above-water topography obtained from field measurements can be evaluated using Pearson correlation  
319 coefficients and  $R^2$ . The results indicate that the consistency between the original and actual  
320 above-water topography is remarkably low, with  $R^2$  values less than 0.2 for both validation wetlands.  
321 Previous studies have also observed significant numerical discrepancies between the original and actual  
322 above-water topography in some regions (e.g., Mukul et al., 2017; Uemaa et al., 2020). Compared to  
323 the original results, the consistency between the corrected and actual above-water topography  
324 significantly improves. For example, the Pearson correlation coefficient and  $R^2$  reach -0.74 and 0.55  
325 in the Baihe Lake, respectively, demonstrating that the WetlandSCB framework can effectively correct  
326 numerical biases in above-water topography.



327

328 Figure 10. (a) and (b) Consistency analysis results between the original and corrected above-water  
329 topography for Baihe Lake. (c) and (d) are corresponding results for Chagan Lake.

330

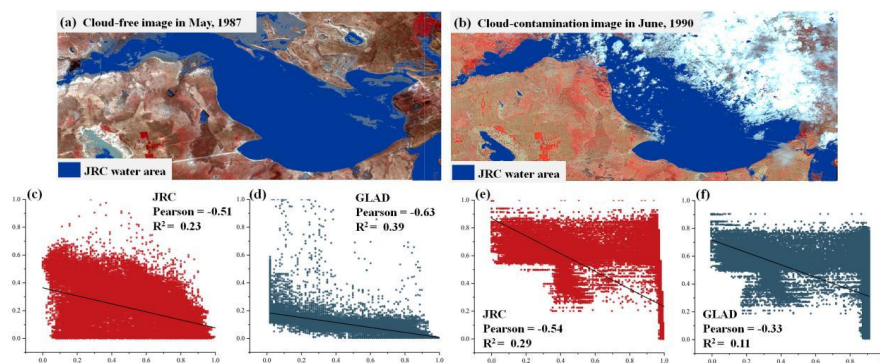
331 Uncertainty in correcting above-water topography using the WetlandSCB framework depends  
332 primarily on the accuracy of the water occurrence map. Therefore, this study analyzed the correlation





333 between two sets of global-scale water occurrence maps, namely GLAD (Pickens et al., 2020) and JRC,  
334 with actual above-water topography. The results show that the correlation level of GLAD is superior to  
335 JRC in the Baihe Lake, while the opposite is observed in the Chagan Lake. Additionally, the  $R^2$  values  
336 for both sets of water occurrence maps are less than 0.4 (Figure 11c-f), which is significantly lower  
337 than the accuracy level of the corrected above-water topography. This clearly shows the superiority of  
338 the water occurrence map generated by the WetlandSCB framework over the GLAD or original JRC  
339 map.

340 It is to note that the water occurrence map generated by the WetlandSCB framework still has a  
341 certain level of uncertainty. First, the extraction of a complete and accurate water spatial distribution  
342 from cloud-free images is constrained by factors such as the classification algorithm (Figure 11a)  
343 (Peket et al., 2016), but some correction algorithms have been proposed to enhance raw water  
344 distribution images (Zhao and Gao, 2018). Second, there is currently a lack of high-precision,  
345 temporally and spatially continuous water distribution maps (Figure 11b). Future efforts could include  
346 the use of image fusion methods, such as the Spatial and Temporal Adaptive Reflectance Fusion Mode,  
347 to fuse data from multi-source remote sensing products such as Sentinel-2, MODIS, and Landsat,  
348 which can effectively enhance the accuracy of water occurrence map (He et al., 2020; Wang et al.,  
349 2016).



350  
351 **Figure 11. (a) and (b) depict sources of uncertainty in water occurrence map generated by the WetlandSCB**  
352 **framework. (c), (d), (e) and (f) illustrate the difference between two water occurrence maps on the**  
353 **performance of above-water topography correction in the Baihe Lake and the Chagan Lake.**

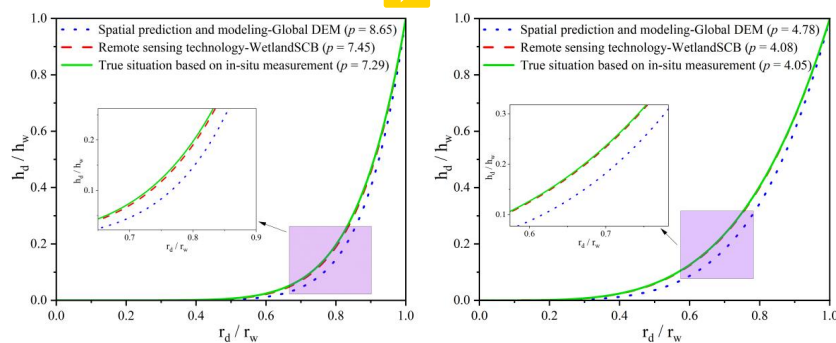
354

### 355 4.3 Performance evaluation of bathymetric information estimation



356 The slope profile  $p$  is used to describe the bathymetry of wetland depressional areas. The  
357 calculated  $p$  values for the Baihe lake and the Chagan Lake using the WetlandSCB framework are 7.45  
358 and 4.08, respectively. The relative errors with respect to the actual  $p$  values obtained from field  
359 measurements are both less than 3%, demonstrating the high accuracy of the framework in estimating  
360 underwater bathymetry.

361 To further prove the superiority of the WetlandSCB framework in estimating bathymetry, this  
362 study employed spatial prediction and modeling methods, resulting in a  $p$  value of 8.65 for the Baihe  
363 Lake and 4.78 for the Chagan Lake. The relative errors with respect to the actual  $p$  values are both  
364 greater than 18%, indicating that this method may lead to substantial errors in some regions, as also  
365 reported by Papa et al. (2013) and Vanthof and Kelly. (2019). Furthermore, previous studies have often  
366 applied smoothing methods to the global DEMs to enhance the accuracy of topographic  
367 characterization in wetland depressions (e.g., Jones et al., 2018; Wu et al., 2019). In this regard, we  
368 further used the Gaussian-smoothed global DEMs and the spatial prediction and modelling methods to  
369 calculate  $p$  for the Baihe Lake and the Chagan Lake. The resulting values were 8.51 and 4.37, with  
370 relative errors of 17.63% and 7.9%, respectively. This underscores that smoothing methods do indeed  
371 contribute to improving the accuracy of topographic information in wetland depressions. Notably, the  
372 relative error for the Chagan Lake is significantly lower than that for the Baihe Lake, which is  
373 consistent with the findings of Liu and Song (2022), who reported that the spatial prediction and  
374 modeling methods are suitable for wetlands with long and narrow shape. In summary, it can be seen  
375 that the WetlandSCB framework excels in the accuracy of estimating bathymetry in wetland  
376 depressional areas when compared to other methods.



377

378 **Figure 12. Slope profile  $p$  values of wetland depressions for the Baihe Lake (left) and the Chagan Lake**

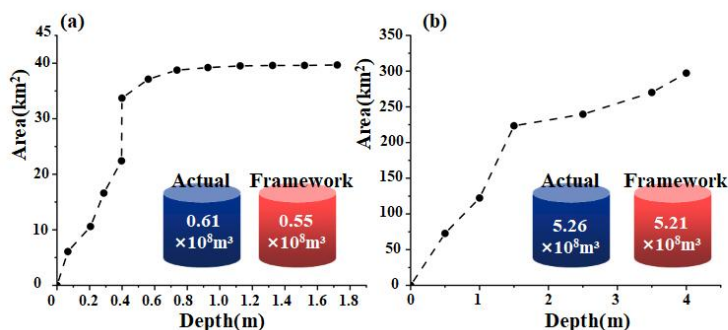


379 (right), calculated with spatial prediction and modeling methods, and the WetlandSCB framework in  
380 comparison with filed measurements.

381

#### 382 4.4 WetlandSCB framework application and implications for integrated water resources 383 management

384 Wetland depressions are largely disregarded in many hydrologic modeling practices. Rare studies  
385 exist on how their exclusion can lead to potentially inaccurate model projections and understanding of  
386 hydrologic dynamics across the world's river basins (Rajib et al., 2020). This study applied a novel  
387 framework delineating the topography and bathymetry of wetland depressional areas and focusing on  
388 two distinctive wetlands to estimate WDWSC. Using the field measurements of topography and  
389 bathymetry of the Baihe Lake and the Chagan Lake, the depth-area hypsometric curves were  
390 constructed, and the WDWSC of the Baihe Lake and the Chagan Lake were estimated to be 61 million  
391 m<sup>3</sup> and 526 million m<sup>3</sup>, respectively (Fig. 13). The estimation results based on the WetlandSCB  
392 framework were correspondingly 55 million m<sup>3</sup> and 521 million m<sup>3</sup>, and the relative errors with the  
393 actual measured WDWSC were both less than 10%, which is a good level of accuracy in estimation  
394 precision (Moriassi et al., 2015). These results demonstrate the ability of the framework to accurately  
395 estimate WDWSC, which can be applied to regions lacking field measurement data for global-scale  
396 wetland water storage capacity estimation.



397

398 Figure 13. The dashed line and blue cylinder represent the actual hypsometric curve and the corresponding  
399 actual WDWSC based on field measurements, respectively. The red cylinder indicates the estimated  
400 WDWSC from the WetlandSCD framework for the Baihe Lake (a) and the Chagan Lake (b).

401



402 Wetlands play a pivotal role in mitigating flood and drought risks, as well as addressing water  
403 scarcity challenge within a river basin. Previous studies underscore the significant impact of wetlands  
404 in attenuating future flood characteristics, including peak flows, mean flows, duration, and flow  
405 volume for various return period floods (Wu et al., 2023). Concurrently, wetlands contribute to  
406 enhancing baseflow during both summer and winter seasons in the NRB (Wu et al., 2020c). Given the  
407 NRB is a agriculture-dominated river basin, wetlands serves as the main water supply nodes by  
408 collecting the flash flood and storing and purifying irrigation return flows. This reclaimed water can be  
409 efficiently reused for irrigation purposes in the NRB (Meng et al., 2019; Smiley and Allred, 2011; Zou  
410 et al., 2018). The WDWSC is a key parameter for evaluating the flood control and water supply  
411 capacity of wetlands, also as a important prerequisite for understanding the impact of wetlands on  
412 extreme hydrological events (Acreman and Holden, 2013). Therefore, the developed WetlandSCB  
413 framework, which can provide accurate estimation of the WDWSC, contributes to the management of  
414 food and water security in the NRB. Against the backdrop of global environmental change,  
415 characterized by an escalation in the intensity and frequency of extreme hydrological events, and the  
416 increasing disparity between water resource supply and demand, there is an urgent need for a novel  
417 integrated water resources management approach based on natural solutions (Rodell and Li, 2023;  
418 Thorslund et al., 2017; Yin et al., 2018). Wetlands have emerged as a nature-based solution in various  
419 water resources management practices (Ferreira et al., 2023). Taking advantage of the wetland  
420 hydrological regulation functions is instrumental in addressing the risks of flood and drought disasters  
421 arising from global climate change, land use change, as well as the water scarcity risks stemming from  
422 agricultural-ecological water competition. This can help develop effective adaptation strategies and  
423 decisions for integrated water resources management.

## 424 5 Conclusions

425 This study developed a novel framework to accurately quantify wetland depression water storage  
426 capacity using coarse-resolution terrain data. The developed framework, WetlandSCB integrates  
427 multi-source remote sensing data, historical maps and prior knowledge, and achieved a high prediction  
428 of wetland depressional distribution and water storage capacity. This is achieved through four steps: 1)  
429 integrating priority-flood algorithm, morphological operators and prior information on water  
430 distribution maps to delineate spatial extent of wetland depressional areas; 2) correcting numerical  
431 biases in above-water topography with water occurrence map; 3) coupling spatial prediction and



432 modeling with remote sensing techniques to estimate bathymetric information, and 4) quantifying  
433 depression area water storage capacity based on depth-area rating curves. The concept and technical  
434 approaches are applicable to large-scale wetland depression water storage estimation, as well as to the  
435 regions where field measurements and/or high-resolution data are not available. Application of the  
436 WetlandSCB framework provides accurate distribution and depth-area relations of wetland  
437 depression areas which can be incorporated into wetland modules of hydrological models (e.g.,  
438 HYDROTEL, SWAT, HYPE, CHRM) to improve the accuracy of flow and storage predictions in river  
439 basins.

440

441 *Data Availability.*

442 The data used in this study are openly available for research purposes. The SRTM DEM and  
443 SRTM Water Body Data can be downloaded at <https://earthexplorer.usgs.gov>. Wetland maps are  
444 available at <https://zenodo.org/records/5816591> and <http://northeast.geodata.cn/index.html>. Water  
445 distribution maps and water occurrence map are available at <https://earthengine.google.com>. Altimetry  
446 satellite data can be downloaded at <https://scihub.copernicus.eu>.

447

448 *Author contribution.*

449 Boting Hu, Liwen chen and Yanfeng Wu designed and executed the study, all authors contributed to  
450 general idea, the discussion and editing of the manuscript.

451

452 *Competing interest.*

453 The authors declare that they have no conflict of interest.

454

455 *Acknowledgments.*

456 This work was supported by the Strategic Priority Research Program of the Chinese Academy of  
457 Sciences, China (XDA28020501), National Natural Science Foundation of China (41877160), National  
458 Key Research and Development Program of China (2017YFC0406003, 2021YFC3200203) and The  
459 Consulting Project Proposal of the Chinese Academy of Engineering (JL2023-17).

460

461 **References**





- 462 Acreman, M. and Holden, J.: How wetlands affect floods, *Wetlands*, 33, 773-786, <https://doi.org/10.1007/s13157-013-0473-2>, 2013.
- 464 Ahmad, S. K., Hossain, F., Pavelsky, T., Parkins, G. M., Yelton, S., Rodgers, M., Little, S., Haldar, D., Ghafoor, S., Khan, R. H., Shawn, N. A., Haque, A., and Biswas, R. K.: Understanding volumetric water storage in monsoonal wetlands of Northeastern Bangladesh, *Water Resour. Res.*, 56(12), e2020WR027989, <https://doi.org/10.1029/2020WR027989>, 2020.
- 466 Aires, F., Miolane, L., Prigent, C., Pham, B., Fluet-Chouinard, E., Lehner, B., and Papa, F.: A global dynamic long-term inundation extent dataset at high spatial resolution derived through downscaling of satellite observations, *J. Hydrometeorol.*, 18(5), 1305-1325, <https://doi.org/10.1175/JHM-D-16-0155.1>, 2017.
- 472 Armon, M., Dente, E., Shmilovitz, Y., Mushkin, A., Cohen, T. J., Morin, E., and Enzel, Y.: Determining bathymetry of shallow and ephemeral desert lakes using satellite imagery and altimetry, *Geophys. Res. Lett.*, 47(7), e2020GL087367, <https://doi.org/10.1029/2020GL087367>, 2020.
- 475 Barnes, R., Lehman, C., and Mulla, D.: Priority-flood: An optimal depression-filling and watershed-labeling algorithm for digital elevation models, *Comput. Geosci.*, 62, 117-127, <https://doi.org/10.1016/j.cageo.2013.04.024>, 2014.
- 478 Bonnema, M., Sikder, S., Miao, Y., Chen, X., Hossain, F., Ara Pervin, I., Mahbubur Rahman, S. M., and Lee, H.: Understanding satellite-based monthly-to-seasonal reservoir outflow estimation as a function of hydrologic controls, *Water Resour. Res.*, 52(5), 4095-4115, <https://doi.org/10.1002/2015WR017830>, 2016.
- 482 Bonnema, M. and Hossain, F.: Inferring reservoir operating patterns across the Mekong Basin using only space observations, *Water Resour. Res.*, 53(5), 3791-3810, <https://doi.org/10.1002/2016WR019978>, 2017.
- 485 Chen, W., Nover, D., Yen, H., Xia, Y., He, B., Sun, W., and Viers, J.: Exploring the multiscale hydrologic regulation of multipond systems in a humid agricultural catchment, *Water Res.*, 184, 115987, <https://doi.org/10.1016/j.watres.2020.115987>, 2020.
- 488 Chu, L., Oloo, F., Sudmanns, M., Tiede, D., Hölbling, D., Blaschke, T., and Teleoaca, I.: Monitoring long-term shoreline dynamics and human activities in the Hangzhou Bay, China, combining daytime and nighttime EO data, *Big Earth Data*, 4(3), 242-264, <https://doi.org/10.1080/20964471.2020.1740491>, 2020.
- 492 Clark, M. P. and Shook, K. R.: The Numerical Formulation of Simple Hysteretic Models to Simulate the Large-Scale Hydrological Impacts of Prairie Depressions, *Water Resour. Res.*, 58(12), e2022WR032694, <https://doi.org/10.1029/2022WR032694>, 2020.
- 495 Cohen, M. J., Creed, I. F., Alexander, L., Basu, N. B., Calhoun, A. J., Craft, C., D'Amico, E., DeKeyser, E., Fowler, L., Golden, H. E., Jawitz, J. W., Kalla, P., Kirkman, L. K., Lane, C. R., Lang, M., Leibowitz, S. G., Lewis, D.B., Marton, J., McLaughlin, D. L., Mushet, D. M., Raanan-Kiperwas, H., Rains, M. C., Smith, L., and Walls, S. C.: Do geographically isolated wetlands influence landscape functions?, *Proc. Natl. Acad. Sci. U. S.A.*, 113(8), 1978-1986, <https://doi.org/10.1073/pnas.1512650113>, 2016.
- 501 De Klerk, A. R., De Klerk, L. P., Oberholster, P. J., Ashton, P. J., Dini, J. A., and Holness, S. D.: A review of depression wetlands (pans) in South Africa, including a water quality classification system, <https://doi.org/10.13140/RG.2.2.28486.06723>, 2016.



- 504 Duan, Z. and Bastiaanssen, W. G. M.: Estimating water volume variations in lakes and reservoirs from four operational satellite altimetry databases and satellite imagery data, *Remote Sens. Environ.*, 134, 403-416, <https://doi.org/10.1016/j.rse.2013.03.010>, 2013.
- 507 Evenson, G. R., Golden, H. E., Lane, C. R., McLaughlin, D. L., and D'Amico, E.: Depression al wetlands affect watershed hydrological, biogeochemical, and ecological functions, *Ecol. Appl.*, 28(4), 953-966, <https://doi.org/10.1002/eap.1701>, 2018.
- 510 Fang, Y., Li, H., Wan, W., Zhu, S., Wang, Z., Hong, Y., and Wang, H.: Assessment of water storage change in China's lakes and reservoirs over the last three decades, *Remote Sens.*, 11(12), 1467, <https://doi.org/10.3390/rs11121467>, 2019.
- 513 Ferreira, C. S., Kašanin-Grubin, M., Solomun, M. K., Sushkova, S., Minkina, T., Zhao, W., and Kalantari, Z.: Wetlands as nature-based solutions for water management in different environments, *Curr. Opin. Environ. Sci. Health*, 100476, <https://doi.org/10.1016/j.coesh.2023.100476>, 2023.
- 517 Gao, H.: Satellite remote sensing of large lakes and reservoirs: From elevation and area to storage, *Wiley Interdisciplinary Reviews: Water*, 2(2), 147-157, <https://doi.org/10.1002/wat2.1065>, 2015.
- 520 Haag, K. H., Lee, T. M., Herndon, D. C., County, P., and Water, T. B.: Bathymetry and vegetation in isolated marsh and cypress wetlands in the northern Tampa Bay area, 2000-2004, U.S. Department of the Interior, US Geological Survey, <https://lccn.loc.gov/2005452253>, 2005.
- 523 Hayashi, M. and Van der Kamp, G.: Simple equations to represent the volume–area–depth relations of shallow wetlands in small topographic depressions, *J. Hydrol.*, 237(1-2), 74-85, [https://doi.org/10.1016/S0022-1694\(00\)00300-0](https://doi.org/10.1016/S0022-1694(00)00300-0), 2000.
- 526 He, D., Zhong, Y., and Zhang, L.: Spectral–spatial–temporal MAP-based sub-pixel mapping for land-cover change detection, *IEEE Trans. Geosci. Remote Sensing*, 58(3), 1696-1717, <https://doi.org/10.1109/TGRS.2019.2947708>, 2019.
- 529 Huang, Q., Li, X., Han, P., Long, D., Zhao, F., and Hou, A.: Validation and application of water levels derived from Sentinel-3A for the Brahmaputra River, *SCI CHINA. TECHNOL SC.*, 1760-1772, <https://doi.org/10.1007/s11431-019-9535-3>, 2019.
- 532 Huang, S., Young, C., Feng, M., Heidemann, K., Cushing, M., Mushet, D. M., and Liu, S.: Demonstration of a conceptual model for using LiDAR to improve the estimation of floodwater mitigation potential of prairie pothole region wetlands, *J. Hydrol.*, 405(3-4), 417-426, <https://doi.org/10.1016/j.jhydrol.2011.05.040>, 2011.
- 536 Jones, C. N., Evenson, G. R., McLaughlin, D. L., Vanderhoof, M. K., Lang, M. W., McCarty, G. W., Golden, E. H., Lane, C.R., and Alexander, L. C.: Estimating restorable wetland water storage at landscape scales, *Hydrol. Process.*, 32(2), 305-313, <https://doi.org/10.1002/hyp.11405>, 2018.
- 540 Kessler, A. C. and Gupta, S. C.: Drainage impacts on surficial water retention capacity of a prairie pothole watershed, *J. Am. Water Resour. Assoc.*, 1-13, <https://doi.org/10.1111/jawr.12288>, 2015.
- 543 Lane, C. R. and D'Amico, E.: Calculating the ecosystem service of water storage in isolated wetlands using LiDAR in North Central Florida, USA, *Wetlands*, 30, 967-977, <https://doi.org/10.1007/s13157-010-0085-z>, 2010.
- 546 Lane, C. R., Leibowitz, S. G., Autrey, B. C., LeDuc, S. D., and Alexander, L. C.: Hydrological, physical, and chemical functions and connectivity of non-floodplain wetlands to downstream





- 548 m waters: A review, *J. Am. Water Resour. Assoc.*, 54(2), 346-371, <https://doi.org/10.1111/1752->  
549 1688.12633, 2018.
- 550 Lindsay, J. B.: Whitebox GAT: A case study in geomorphometric analysis, *Comput. Geosci*, 95,  
551 75-84, <https://doi.org/10.1016/j.cageo.2016.07.003>, 2016.
- 552 Liu, K. and Song, C.: Modeling lake bathymetry and water storage from DEM data constrain-  
553 ed by limited underwater surveys, *J. Hydrol.*, 604, 127260, <https://doi.org/10.1016/j.jhydrol.2021.>  
554 127260, 2022.
- 555 Liu, K., Song, C., Zhan, P., Luo, S., and Fan, C.: A Low-Cost Approach for Lake Volume Est-  
556 imation on the Tibetan Plateau: Coupling the Lake Hypsometric Curve and Bottom Elevatio-  
557 n, *Front. Earth Sci.*, 10, 925944, <https://doi.org/10.3389/feart.2022.925944>, 2022.
- 558 Liu, K., Song, C., Zhao, S., Wang, J., Chen, T., Zhan, P., Fan, C., and Zhu, J.: Mapping inun-  
559 dated bathymetry for estimating lake water storage changes from SRTM DEM: A global inve-  
560 stigation., *Remote Sens. Environ.*, 301, 113960, <https://doi.org/10.1016/j.rse.2023.113960>, 2024.
- 561 Li, X., Ling, F., Foody, G. M., Boyd, D. S., Jiang, L., Zhang, Y., Zhou, P., Wang, Y., Chen,  
562 R., and Du, Y.: Monitoring high spatiotemporal water dynamics by fusing MODIS, Landsat,  
563 water occurrence data and DEM, *Remote Sens. Environ.*, 265, 112680, <https://doi.org/10.1016/j.>  
564 rse.2021.112680, 2021.
- 565 Li, X., Long, D., Huang, Q., Han, P., Zhao, F., and Wada, Y.: High-temporal-resolution water l-  
566 evel and storage change data sets for lakes on the Tibetan Plateau during 2000–2017 using m-  
567 ultiple altimetric missions and Landsat-derived lake shoreline positions, *Earth Syst. Sci. Dat-*  
568 *a*, 11(4), 1603-1627, <https://doi.org/10.5194/essd-11-1603-2019>, 2019a.
- 569 Li, Y., Gao, H., Jasinski, M. F., Zhang, S., and Stoll, J. D.: Deriving high-resolution reservoir  
570 bathymetry from ICESat-2 prototype photon-counting lidar and landsat imagery, *IEEE Trans.*  
571 *Geosci. Remote Sensing*, 57(10), 7883-7893, <https://doi.org/10.1109/TGRS.2019.2917012>, 2019  
572 b.
- 573 Luo, S., Song, C., Liu, K., Ke, L., and Ma, R.: An effective low-cost remote sensing approac-  
574 h to reconstruct the long-term and dense time series of area and storage variations for large l-  
575 akes, *Sensors*, 19(19), 4247, <https://doi.org/10.3390/s19194247>, 2019.
- 576 Mao, D., Wang, Z., Du, B., Li, L., Tian, Y., Jia, M., Zeng, Y., Song, K., Jiang, M., and Wang,  
577 Y.: National wetland mapping in China: A new product resulting from object-based and hier-  
578 archical classification of Landsat 8 OLI images, *ISPRS-J. Photogramm. Remote Sens.*, 164, 11  
579 -25, <https://doi.org/10.1016/j.isprsjprs.2020.03.020>, 2020.
- 580 Meng, B., Liu, J. L., Bao, K., and Sun, B.: Water fluxes of Nenjiang River Basin with ecolog-  
581 ical network analysis: Conflict and coordination between agricultural development and wetland  
582 restoration, *J. Clean Prod.*, 213, 933-943, <https://doi.org/10.1016/j.jclepro.2018.12.243>, 2019.
- 583 Messenger, M. L., Lehner, B., Grill, G., Nedeva, I., and Schmitt, O.: Estimating the volume and  
584 age of water stored in global lakes using a geo-statistical approach, *Nat. Commun.*, 7, 136  
585 03, <https://doi.org/10.1038/ncomms13603>, 2016.
- 586 Moriasi, D. N., Gitau, M. W., Pai, N., and Daggupati, P.: Hydrologic and water quality models:  
587 Performance measures and evaluation criteria, *Trans. ASABE*, 58(6), 1763-1785, <https://doi.or>  
588 [g/10.13031/trans.58.10715](https://doi.org/10.13031/trans.58.10715), 2015.
- 589 Mukul, M., Srivastava, V., Jade, S., and Mukul, M.: Uncertainties in the shuttle radar topograp-  
590 hy mission (SRTM) Heights: Insights from the Indian Himalaya and Peninsula, *Sci Rep.*, 7(1),  
591 41672, <https://doi.org/10.1038/srep41672>, 2017.



- 592 Papa, F., Frappart, F., Güntner, A., Prigent, C., Aires, F., Getirana, A. C., and Maurer, R.: Surfa  
593 ce freshwater storage and variability in the Amazon basin from multi-satellite observations, 1  
594 993–2007, *J. Geophys. Res.-Atmos*, 118(21), 11-951, <https://doi.org/10.1002/2013JD020500>, 201  
595 3.
- 596 Pekel, J. F., Cottam, A., Gorelick, N., and Belward, A. S.: High-resolution mapping of global  
597 surface water and its long-term changes, *Nature*, 540(7633), 418-422, <https://doi.org/10.1038/nature20584>, 2016.
- 599 Pickens, A. H., Hansen, M. C., Hancher, M., Stehman, S. V., Tyukavina, A., Potapov, P., Marr  
600 oquin, B., and Sherani, Z.: Mapping and sampling to characterize global inland waterdynami  
601 cs from 1999 to 2018 with full Landsat time-series, *Remote Sens. Environ*, 243,111792, <https://doi.org/10.1016/j.rse.2020.111792>, 2020.
- 603 Pulvirenti, L., Chini, M., Pierdicca, N., Guerriero, L., and Ferrazzoli, P.: Flood monitoring using  
604 multi-temporal COSMO-SkyMed data: Image segmentation and signature interpretation, *Rem  
605 ote Sens. Environ*, 115(4), 990-1002, <https://doi.org/10.1016/j.rse.2010.12.002>, 2011a.
- 606 Pulvirenti, L., Pierdicca, N., Chini, M., and Guerriero, L.: An algorithm for operational flood  
607 mapping from Synthetic Aperture Radar (SAR) data using fuzzy logic, *Nat. Hazards Earth Sy  
608 st. Sci*, 11(2), 529-540, <https://doi.org/10.5194/nhess-11-529-2011>, 2011b.
- 609 Rajib, A., Golden, H. E., Lane, C. R., and Wu, Q.: Surface depression and wetland water stora  
610 ge improves major river basin hydrologic predictions, *Water Resour. Res*, 56(7), e2019WR026  
611 561, <https://doi.org/10.1029/2019WR026561>, 2020.
- 612 Rodell, M. and Li, B.: Changing intensity of hydroclimatic extreme events revealed by GRAC  
613 E and GRACE-FO, *Nat. Water*, 1(3), 241-248, <https://doi.org/10.1038/s44221-023-00040-5>, 202  
614 3.
- 615 Shook, K., Papalexiou, S., and Pomeroy, J. W.: Quantifying the effects of Prairie depressiona  
616 l storage complexes on drainage basin connectivity, *J. Hydrol*, 593, 125846, <https://doi.org/10.1016/j.jhydrol.2020.125846>, 2021.
- 618 Sjöberg, Y., Dessirier, B., Ghajarnia, N., Jaramillo, F., Jarsjö, J., Panahi, D. M., Xu, D., Zou,  
619 L., and Manzoni, S.: Scaling relations reveal global and regional differences in morphometry  
620 of reservoirs and natural lakes, *Sci. Total Environ*, 822, 153510, <https://doi.org/10.1016/j.scitotenv.2022.153510>, 2022.
- 622 Smiley Jr, P. C. and Allred, B. J.: Differences in aquatic communities between wetlands create  
623 d by an agricultural water recycling system, *Wetl. Ecol. Manag.*, 19(6), 495-505, <https://doi.org/10.1007/s11273-011-9231-5>, 2011.
- 625 Thorslund, J., Jarsjö, J., Jaramillo, F., Jawitz, J. W., Manzoni, S., Basu, N. B., Chalov, M.J., C  
626 reed, I. F., Goldenberg, R., Hysin, A., Kalantari, Z., Koussis, A. D., Lyon, S. W., Mazi, K.,  
627 Mard, J., Persson, K., Pietro, J., Prieto, C., Quin, A., and Destouni, G.: Wetlands as large-sc  
628 ale nature-based solutions: Status and challenges for research, engineering and management, *Ec  
629 ol. Eng*, 108, 489-497, <https://doi.org/10.1016/j.ecoleng.2017.07.012>, 2017.
- 630 Tsai, J. S., Venne, L. S., McMurry, S. T., and Smith, L. M.: Vegetation and land use impact o  
631 n water loss rate in playas of the Southern High Plains, USA, *Wetlands*, 30, 1107-1116, <https://doi.org/10.1007/s13157-010-0117-8>, 2010.
- 633 Uuemaa, E., Ahi, S., Montibeller, B., Muru, M., and Knoch, A.: Vertical accuracy of freely av  
634 ailable global digital elevation models (ASTER, AW3D30, MERIT, TanDEM-X, SRTM, and N  
635 ASADEM), *Remote Sens.*, 12(21), 3482, <https://doi.org/10.3390/rs12213482>, 2020.



- 636 Vanthof, V. and Kelly, R.: Water storage estimation in ungauged small reservoirs with the Tan  
637 DEM-X DEM and multi-source satellite observations, *Remote Sens. Environ.*, 235, 111437, <https://doi.org/10.1016/j.rse.2019.111437>, 2019.
- 639 Verones, F., Pfister, S., and Hellweg, S.: Quantifying area changes of internationally important  
640 wetlands due to water consumption in LCA, *Environ. Sci. Technol.*, 47(17), 9799-9807, <https://doi.org/10.1021/es400266v>, 2013.
- 642 Wang, Q., Shi, W., and Atkinson, P. M.: Spatiotemporal subpixel mapping of time-series image  
643 s, *IEEE Trans. Geosci. Remote Sensing*, 54(9), 5397-5411, <https://doi.org/10.1109/TGRS.2016.2562178>, 2016.
- 645 Wu, Q., Lane, C. R., Wang, L., Vanderhoof, M. K., Christensen, J. R., and Liu, H.: Efficient  
646 delineation of nested depression hierarchy in digital elevation models for hydrological analysis  
647 using level-set method, *J. Am. Water Resour. Assoc.*, 55(2), 354-368, <https://doi.org/10.1111/1752-1688.12689>, 2019.
- 649 Wu, Q. and Lane, C. R.: Delineation and quantification of wetland depressions in the Prairie P  
650 othole Region of North Dakota, *Wetlands*, 36(2), 215-227, <https://doi.org/10.1007/s13157-015-0731-6>, 2016.
- 652 Wu, Y., Sun, J., Blanchette, M., Rousseau, A. N., Xu, Y. J., Hu, B., and Zhang, G.: Wetland  
653 mitigation functions on hydrological droughts: From drought characteristics to propagation of  
654 meteorological droughts to hydrological droughts, *J. Hydrol.*, 617, 128971, <https://doi.org/10.1016/J.JHYDROL.2022.128971>, 2023.
- 656 Wu, Y., Sun, J., Xu, Y. J., Zhang, G., and Liu, T.: Projection of future hydrometeorological ex  
657 tremes and wetland flood mitigation services with different global warming levels: A case st  
658 udy in the Nenjiang river basin, *Ecol. Indic.*, 140, 108987, <https://doi.org/10.1016/j.ecolind.2022.108987>, 2022a.
- 660 Wu, Y., Zhang, G., Rousseau, A. N., and Xu, Y. J.: Quantifying streamflow regulation services  
661 of wetlands with an emphasis on quickflow and baseflow responses in the Upper Nenjiang  
662 River Basin, Northeast China, *J. Hydrol.*, 583, 124565, <https://doi.org/10.1016/j.jhydrol.2020.124565>, 2020b.
- 664 Wu, Y., Zhang, G., Rousseau, A. N., Xu, Y. J., and Foulon, É.: On how wetlands can provide  
665 flood resilience in a large river basin: a case study in Nenjiang river Basin, China, *J. Hydro*  
666 *l.*, 587, 125012, <https://doi.org/10.1016/j.jhydrol.2020.125012>, 2020c.
- 667 Xiong, L., Tang, G., Yang, X., and Li, F.: Geomorphology-oriented digital terrain analysis: Progr  
668 ess and perspectives, *J. Geogr. Sci.*, 31, 456-476, <https://doi.org/10.1007/s11442-021-1853-9>, 2  
669 021.
- 670 Yang, J. and Huang, X.: 30 m annual land cover and its dynamics in China from 1990 to 20  
671 19, *Earth Syst. Sci. Data*, 2021, 1-29, <https://doi.org/10.5194/essd-13-3907-2021>, 2021.
- 672 Yao, F., Wang, J., Wang, C., and Crétaux, J. F.: Constructing long-term high-frequency time se  
673 ries of global lake and reservoir areas using Landsat imagery, *Remote Sens. Environ.*, 232, 11  
674 1210, <https://doi.org/10.1016/j.rse.2019.111210>, 2019.
- 675 Yao, F., Wang, J., Yang, K., Wang, C., Walter, B. A., and Crétaux, J. F.: Lake storage variatio  
676 n on the endorheic Tibetan Plateau and its attribution to climate change since the newmillen  
677 nium, *Environ. Res. Lett.*, 13(6), 064011, <https://doi.org/10.1088/1748-9326/aab5d3>, 2018.



- 678 Yin, J., Gentine, P., Zhou, S., Sullivan, S. C., Wang, R., Zhang, Y., and Guo, S.: Large increa  
679 se in global storm runoff extremes driven by climate and anthropogenic changes, *Nat. Commu*  
680 *n.* 9(1), 4389, <https://doi.org/10.1038/s41467-018-06765-2>, 2018.
- 681 Zhang, X., Liu, L., Chen, X., Gao, Y., Xie, S., and Mi, J.: GLC\_FCS30: Global land-cover pr  
682 oduct with fine classification system at 30 m using time-series Landsat imagery, *EarthSyst. S*  
683 *ci. Data*, 13(6), 2753-2776, <https://doi.org/10.5194/essd-13-2753-2021>, 2021.
- 684 Zhao, G. and Gao, H.: Automatic correction of contaminated images for assessment of reservoi  
685 r surface area dynamics, *Geophys. Res. Lett.* 45(12), 6092-6099, [https://doi.org/10.1029/2018G](https://doi.org/10.1029/2018GL078343)  
686 [L078343](https://doi.org/10.1029/2018GL078343), 2018.
- 687 Zhou, G., Sun, Z., and Fu, S.: An efficient variant of the priority-flood algorithm for filling d  
688 epressions in raster digital elevation models, *Comput. Geosci*, 90, 87-96, [https://doi.org/10.1016](https://doi.org/10.1016/j.cageo.2016.02.021)  
689 [/j.cageo.2016.02.021](https://doi.org/10.1016/j.cageo.2016.02.021), 2016.
- 690 Zou, Y., Wang, L., Xue, Z., E, M., Jiang, M., Lu, X., Yang, S., Shen, X., Liu, Z., Sun, G., a  
691 nd Yu, X.: Impacts of agricultural and reclamation practices on wetlands in the AmurRiver  
692 Basin, Northeastern China, *Wetlands*, 38, 383-389, <https://doi.org/10.1007/s13157-017-0975-4>, 2  
693 018.
- 694 Zou, Z., Xiao, X., Dong, J., Qin, Y., Doughty, R. B., Menarguez, M. A., Zhang, C., and Wan  
695 g, J.: Divergent trends of open-surface water body area in the contiguous United States from  
696 1984 to 2016, *Proc. Natl. Acad. Sci. U. S. A.* 115(15), 3810-3815, [https://doi.org/10.1073/pna](https://doi.org/10.1073/pnas.1719275115)  
697 [s.1719275115](https://doi.org/10.1073/pnas.1719275115), 2018.